ORIGINAL ARTICLE

FFEMS Fatigue & Fracture of Engineering Materials & Structures WILEY

Fatigue strength evaluation of case-hardened components combining heat-treatment simulation and probabilistic approaches

Valérian Iss[1] | Jean-André Meis[2] | Ali Rajaei[1] | Bengt Hallstedt[1] ![ORCID] |
Christoph Broeckmann[1]

[1]Chair and Institute for Materials Applications in Mechanical Engineering, RWTH Aachen University, Aachen, Germany

[2]Flender GmbH, Bocholt, Germany

Correspondence
Valérian Iss, Chair and Institute for Materials Applications in Mechanical Engineering, RWTH Aachen University, Augustinerbach 4, Aachen 52062, Germany.
Email: v.iss@iwm.rwth-aachen.de

Abstract

In order to raise the hardness and strength of the surface layer of mechanical components and induce favorable residual compressive stresses, case-hardening procedures have become established in the heat treatment of steel. In this work, a calculation concept for the fatigue strength of components that have been case-hardened through carburizing heat treatment is being developed. The residual stress and the load stresses in complex-shaped, carburized materials are determined using a finite element (FE) model. The fatigue limit of the components is derived using probabilistic methods and taking into account hardness gradients, residual stresses, and non-metallic inclusions. The model is validated with available axial bending fatigue test data and then used to predict the rotating bending fatigue limit of samples with various geometries and heat-treatment conditions. This work demonstrates the capability of combining probabilistic and FE-based modeling to represent complex interactions between variables that affect the fatigue of heat-treated components, such as steel cleanliness, notch shape, case-hardening depth, or loading conditions.

KEYWORDS
case hardening, fatigue limit, finite-element simulation, non-metallic inclusions, probabilistic method, residual stresses

Highlights

- Combined FE-based and probabilistic methods can predict fatigue strength accurately.
- Interplay of heat-treatment output, geometry, load, and material is considered.
- Crack initiation position gets shifted by increased case-hardness depth.
- Fatigue strength reduction due to defects in steel depends on load concentration.

1 | INTRODUCTION

In many mechanical engineering applications, the surface layer of components experiences the highest mechanical load. In order to specifically raise the hardness and strength of the surface layer as well as often create a favorable residual compressive stress condition, case-hardening procedures have become established in the heat treatment of steel.[1,2] Carburizing is a typical case-hardening heat treatment for heavily loaded components, during which the external surface is enriched in carbon, thus developing, under adequate quenching and tempering conditions, a hard case layer of martensite with compressive residual stresses, while the lower-carbon core of the component retains sufficient ductility. Additionally, further strengthening of highly stressed components can be obtained by subsequent mechanical processes such as shot peening.[1]

The prediction of fatigue properties of case-hardened components is a very complex problem in which many influencing factors are involved. In addition to the graded strength properties induced by the heat treatment, the properties of the external loading (e.g., stress gradient, stress amplitude, mean stress, multiaxiality ...), the component surface (oxidation, roughness), the residual stresses (from heat treatment, shot peening, or finishing process), the component geometry (notch effect, size effect), and the material quality (internal notch effect due to defects and non-metallic inclusions) should also be considered.[3–5]

Because of this, it is expected that only locally based methods will result in a satisfactory framework for determining the fatigue properties of carburized components. The majority of methods compare the locally permissible load amplitude with the local stresses at a specified location.[4] The first methods were described by Lang as early as the 1970s, and they involved developing guidelines based on the description of load stress and local hardness values to estimate the fatigue strength of carburized, induction-hardened, or nitrided components.[6] Numerous studies supported the method's viability and refined the proposed strategy by adding some extra features, modifying the calculation formulas for the many variables involved such as mean stress sensitivity, axial fatigue strength, or notch effect.[4,7–9] While early work by, for example, Velten and Lang is partially included into standards like FKM and ISO 6336, more recent work has not yet been taken into account.[6,10–14]

Size effects describe the differences in the fatigue behavior of geometrically similar samples that have different sizes. In most cases, experimental results from fatigue tests that are conducted on variously sized specimens or components do not agree. When fatigue data from smaller specimens are applied to larger ones, the material's performance is typically overestimated; that is, the fatigue strength falls with increasing component size.[15] Larger stressed volumes increase the probability of finding a flaw or crack in the microstructure that is large enough to trigger crack propagation. This is the statistical size effect. In high-strength materials and for fatigue failures triggered by defects, it is expected that the statistical size effect predominates over other size influences.[16] The highly stressed volume (HSV), which is closely related to stress gradients and frequently defined as the region in which 90% of the actual local maximum stress is exceeded, has been shown to correlate with the expected decrease in fatigue strength due to scaling of a specimen or part.[17] Other assessment approaches typically include using the Weibull weakest link model, which was originally developed for brittle materials and assumes a statistical distribution of defects in the volume or on the surface of a component, with the largest defect being responsible for the start of a fatigue crack that can propagate and eventually cause the component to fail.[18] In the last decade, probabilistic methods for predicting the fatigue strength of parts with statistical size effects have been developed and successfully applied, some of them in the context of case-hardened components.[19–21]

Even though calculation methods have made it possible to significantly increase component power density or reduce costs through optimized design, there remains a research need in this area since carburized parts usually count as key components in mechanical systems such as wind turbines and aerospace propulsion systems, and potential improvements in fatigue life or production routes could have significant economic implications.[2]

One can list the following examples of circumstances for which the models from standards and literature are only partially satisfactory:

- The assessment of residual stresses from carburizing heat treatments is still over-simplified in many cases. Residual stresses belong to the most influential parameters for fatigue strength of components, with tensile residual stresses in the loaded area having a significant negative impact on load capacity and compressive residual stresses inhibiting crack formation. For surface-near compressive residual stresses in case-hardened components, calculation formulas based on empirical data have been created and appear to produce satisfactory results, at least in a limited application range.[6] Only a very small number of experimental residual stress data are, however, accessible in the depth of carburized parts since they require highly sophisticated measurement methods and equipment.[22–25] As a result, there is no generally used

—WILEY—

calculation method available for residual stress in the depth of components that have been carburized. This is made more of an issue by the reports of numerous fatigue failures of carburized components in the last decades that appear to involve tensile residual stresses in the subsurface region but which cannot be assessed using the majority of state-of-the-art methods.[24–26]

- Very few works take the influence of material quality into account. A general framework for calculation of the fatigue strength of carburized components for different steel cleanliness is not available yet. Intensive research work has enabled the design and the admissible load of carburized gears according to the guidelines in International Standardization Organization[13] to be adapted as a function of the material quality. Such a feature is, however, not included in the broader calculation frameworks of DIN 743 or FKM,[12,14] although the quality of the steel partly determines fatigue properties of carburized parts, for example, through cracks initiated at material defects such as non-metallic inclusions.

- The consideration of interactions between the most important influencing factors on the fatigue strength of carburized components is often very coarse and consists of separately estimating the influences of, for example, strengthening due to heat treatment, reduction of the load capability because of surface roughness or tensile mean stress. As a matter of fact, empirical and theoretical studies demonstrate that the majority of parameters that affect the fatigue life of carburized components have a strong reciprocal influence and that it is important to take into account their interactions. Such scenarios were already emphasized in the work of Velten and Kloos,[10,11] who demonstrated that the effect of the heat treatment for case hardening was much greater for round samples when these were notched or loaded under rotating bending than when they were unnotched or loaded with axial tensile-compressive loads. This is explained by the stress concentrations arising at different positions and volumes in the samples and demonstrates that the increase in fatigue strength caused by heat treatment of carburized components can only be predicted with a linked consideration of geometry and load properties. Likewise, it has been noted that, for instance, non-metallic inclusions play a larger role as the loaded volume of a carburized component increases.[27,28]

In this work, the authors develop a methodology to predict the fatigue limit of carburized components. Separate finite element (FE) models are used to calculate residual stress from heat treatment and fatigue load stresses. The fatigue strength of the components is then derived using probabilistic methods, taking non-metallic inclusions, local hardness, and local residual stress values into account. The model is validated using available axial bending fatigue test data and then used to predict the rotating bending fatigue limit of samples with various geometries and heat-treatment conditions. FE-based heat-treatment simulation models allow for precise measurement of local hardness and residual stresses in complex shaped carburized parts while accounting for individual process conditions. The combination with a probabilistic approach for fatigue strength thus appears promising in order to assess the effects of material quality and the interactions between the main influencing factors for fatigue strength. This work is based on previously developed methods for simulating the carburizing heat treatment and for predicting fatigue strength using a probabilistic approach. However, using versatile FE models to provide the probabilistic fatigue model with quantitative estimations of the influencing factors local hardness and local residual stress is, to the authors' knowledge, a new feature that opens up new possibilities in the field of design of heat-treated components as well as tailoring carburizing processes towards optimized fatigue properties.

2 | DEVELOPMENT OF A SIMULATIVE AND PROBABILISTIC APPROACH FOR PREDICTION OF FATIGUE STRENGTH OF CARBURIZED COMPONENTS

2.1 | Simulation of the case-hardening heat treatment

Multi-physical simulation approaches have already proven to be a viable way to determine residual stresses in heat treatments. The FE method has been utilized successfully to calculate residual stress depth profiles for simple processes and geometries as well as for more complex thermal-metallurgical processes.[5,29–33] In contrast to measurements, simulations can be used to carry out parameter studies on the main influences on the residual stress distribution in a very cost-effective way. Today, commercial software packages (e.g., Sysweld, Abaqus, or Dante) already exist to determine residual stresses in components. Since residual stress measurement data for in-depth position are difficult to obtain, FE simulation belongs to the very few methods that enable the determination of the residual stress in carburized components with complex geometries or the investigation of the impact of the carburizing process conditions on the residual stresses. Some recent work even demonstrated the
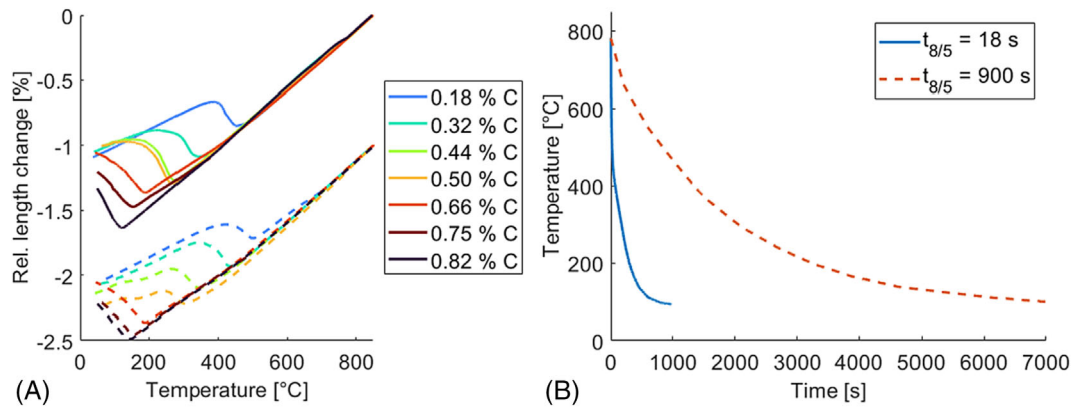
FIGURE 1 Example of experimental data from dilatometer measurements used in Iss et al.[25] to model the phase transformation behavior of steel 18CrNiMo7-6 depending on the carbon concentration and the cooling conditions. Continuous lines correspond to samples quenched with a cooling time between 800°C and 500°C $t_{8/5}$ = 18 s. Dashed lines represent cooling conditions with a characteristic cooling time of 900 s. (A) Relative length changes of dilatometer samples (shifted by −1% for clarity). (B) Corresponding cooling curves of the samples. [Colour figure can be viewed at wileyonlinelibrary.com]

possibility to directly integrate FE-based heat-treatment models in calculation tools for fatigue limit prediction of case-hardened components, thus allowing to adjust mechanical design with heat-treatment routes.[5,34,35]

An FE-based heat-treatment model for case hardening of 18CrNiMo7-6 steel parts was presented in Iss et al.[25] based on the methods described in Eser et al.[32,33] Along with the published thermal-physical parameters from the literature,[36] the researchers used extensive dilatometric investigations of the material's carbon-dependent mechanical and phase-transformation behavior. Modeling the strain development as a function of position and time during quenching and tempering of carburized components allowed for the macro-scale prediction of residual stresses caused by heat treatment. Multiple X-ray residual stress measurements taken in the depth of carburized spur gears were used to validate the model. All examined configurations, which featured significant variations in gear size, case-hardness depth (CHD), quenching medium, and carbon profile, were predicted accurately to a moderate to high degree. Furthermore, the tensile residual stresses in the subsurface region of carburized gears could be described with high precision by the FE model. The FE model is based on the description of the total strain ε^{total} as the superposition of several independent strain components for elastic ε^{el}, plastic ε^{pl}, thermal ε^{th}, transformation ε^{tr}, transformation-induced plasticity ε^{trip}, and creep ε^{cr} strain components, as stated in Equation (1).

$$\varepsilon^{total} = \varepsilon^{el} + \varepsilon^{pl} + \varepsilon^{th} + \varepsilon^{tr} + \varepsilon^{trip} + \varepsilon^{cr} \quad (1)$$

With specially created FORTRAN subroutines to implement the complex material behavior, the FE

problem is solved in the commercial program Abaqus 2020.[37] The elastic strains result of Hooke's law based on the temperature-dependent Young's modulus and Poisson's ratio from Lütjens et al.[38] Flow curves determined under axial compression tests in deformation dilatometer enable a description of the plastic strains using a von Mises yield surface and isotropic hardening. The thermal, transformation, and transformation-induced strains are modeled using the extensive collected dilatometric data as a function of temperature, cooling rate, and carbon concentration. Phase transformations of quenched austenite into ferrite, pearlite, bainite, or martensite are calculated incrementally using calibrated models from the work of Johnson–Mehl–Avrami–Kolmogrow and Koistinen–Marburger.[39–41]

Figure 1A presents the measured relative length variations of 18CrNiMo7-6 steel samples as a function of carbon content for two different cooling speeds, with the associated cooling curves shown in Figure 1B. The evolution of the stresses in the steel as a function of cooling conditions and carbon content can be understood with the use of additional metallographic analysis and X-ray diffraction from Iss et al.[25] Even during rapid cooling, austenite can transform into bainite in the base material with 0.18%C. In the carburized samples, martensite is increasingly formed instead. With increasing carbon concentration, however, the martensitic transformation is not fully completed and leads to substantial residual austenite contents. For defined cooling conditions, the carbon content also affects the morphology of both martensite and bainite phases. With increasing carbon content, the martensitic structure transitions from lath to plate.[25] Carbon concentration also has a significant impact on the transformation behavior under slower cooling conditions, as shown in Figure 1 for $t_{8/5}$ = 900 s.

The formation of ferrite and pearlite can be observed in samples that were not carburized. On the other hand, a sample containing 0.32%C entirely transforms into bainite. With increasing carbon concentration, the bainite formation takes place at lower temperatures, which leads to an evolution of the bainite structure from upper bainite to lower bainite.[25] In carbon-rich materials, hardly any bainite is formed, even at very low cooling rates. The samples with the highest carbon content (0.66%C, 0.75% C, and 0.82%C) exhibit a martensitic structure with retained austenite.

User-defined subroutines are developed to model both phase transformation kinetics and the evolution of the strains ε^{th} and ε^{tr} based on the analysis of the length changes and the microstructure using optical microscopy and X-ray diffraction. Quenching experiments in deformation dilatometer under additional axial compression load enable to characterize the transformation-induced plasticity of martensite and bainite phase transformations and to derive a model for the strains ε^{trip} using the constitutive equations in.[42,43] Creep-induced strains ε^{cr} are neglected in the present study. Based on the experimental data and models from Franz et al. and Lütjens et al.[31,38] as well as hardness measurements on martensite samples before and after tempering, a model is developed to predict the local hardness in carburized components. In this work, the FE-based heat-treatment model is used in order to predict the local hardness and residual stresses in carburized samples. Additional details on the model development are provided in Iss et al.,[25] and similar methodologies can be found in various other works.[30,31,33]

2.2 | Probabilistic calculation of the fatigue strength of carburized samples

Even though the significance of material defects and non-metallic inclusions in the onset of cracks has been noted in earlier research, it is still difficult to account for this feature in numerical models that determine the fatigue strength of carburized components, despite some progress being made in this area recently.[20,27,28] Meis et al.[21] proposed a method featuring explicit modeling of the non-metallic inclusions in a macroscopic loaded component. The approach is novel in that a stochastic distribution of the positions and sizes of the steel's defects is taken into account, and the Murakami-derived principles[16] are then used to update the local admissible stresses. The ability to obtain statistically meaningful fatigue strengths on a component level is made possible by iterations on the random assignment of the positions and sizes of the defects. The general framework of this

approach is shown in Figures 2 and 3. The strength assessment is divided into two calculation steps. In the first step, the maximum strength in the defect-free condition is computed, and in the second step, a Monte Carlo simulation is used to determine the failure probability for a given external load. Individual components are modeled in the Monte Carlo simulation using a distribution of non-metallic inclusions, and the corresponding fatigue strength for each component is calculated. This allows for the estimation of the cumulative distribution function of the fatigue strength for a specific component state.

The geometry of the component is discretized first in the process. Time-dependent stress tensor, residual stresses, and local hardness value should be specified for each material point. While analytical methods can be utilized for simple geometries and load states, FE-based models fit here particularly well to forecast position-dependent stress evolution in notched components. FE simulation models can also be used to calculate the local hardness and residual stress values during the carburizing heat treatment.

The time-dependent multiaxial stresses should be summed up as equivalent stress amplitudes and equivalent mean stresses, where residual stresses are treated as additional mean stresses, as is typical in local-based fatigue strength assessments.[4] The local acceptable load amplitude under uniaxial fatigue loading can be compared to these equivalent stresses by plotting them for each material point in a Haigh diagram. The local hardness, which can be determined via either FE-simulation of the heat treatment, an empirical formula as a function of depth, or user input, is used to calculate the boundaries in the Haigh-diagram. According to Equation (2), which is specified in Murakami[16] and derived from the work of Garwood et al.,[44] an upper bound is defined based on the local hardness in order to estimate the local fatigue strength under fully reversed load for a hypothetical defect-free material state. In order to determine the most vulnerable position for crack initiation in a perfect defect-free state, one must first determine which material point in the component exhibits the largest degree of utilization, which is defined by the ratio of the equivalent stress amplitude to the local acceptable stress amplitude. When non-metallic inclusions are ignored, the fatigue strength of the carburized part is then calculated by scaling the mechanical forces acting on the entire component until the maximum ratio between local equivalent stress amplitude and local admissible stress amplitude reaches 1.

$$\sigma_{wu} = 1.6 \cdot HV \tag{2}$$

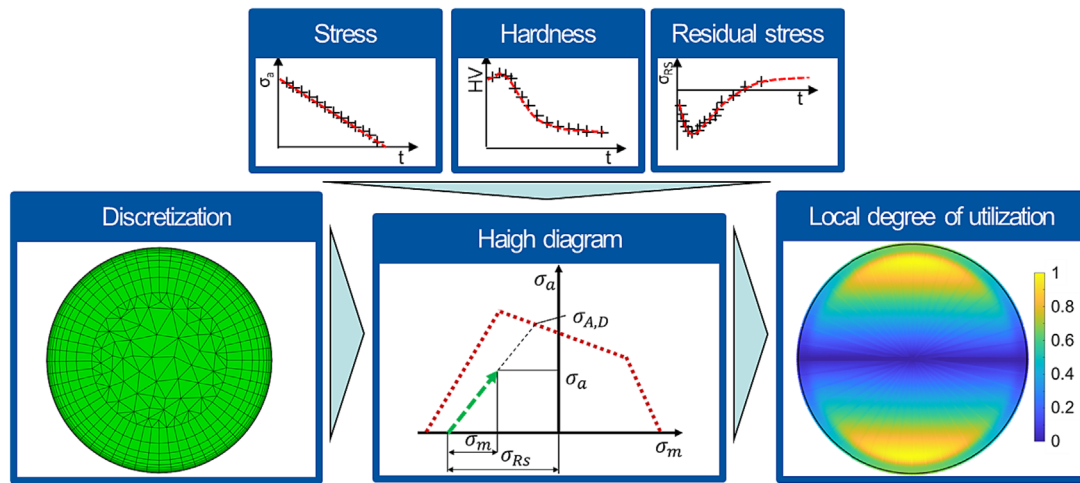In a second step, the effect of material defects on the fatigue strength of the carburized component is

FIGURE 2 Input variables and schematic calculation procedure for the fatigue strength of carburized samples according to Meis et al.[21] for the defect-free component state, using the example of the circular cross section of an unnotched round sample under axial bending loading. The detailed calculation procedure can be found in Appendix A. [Colour figure can be viewed at wileyonlinelibrary.com]
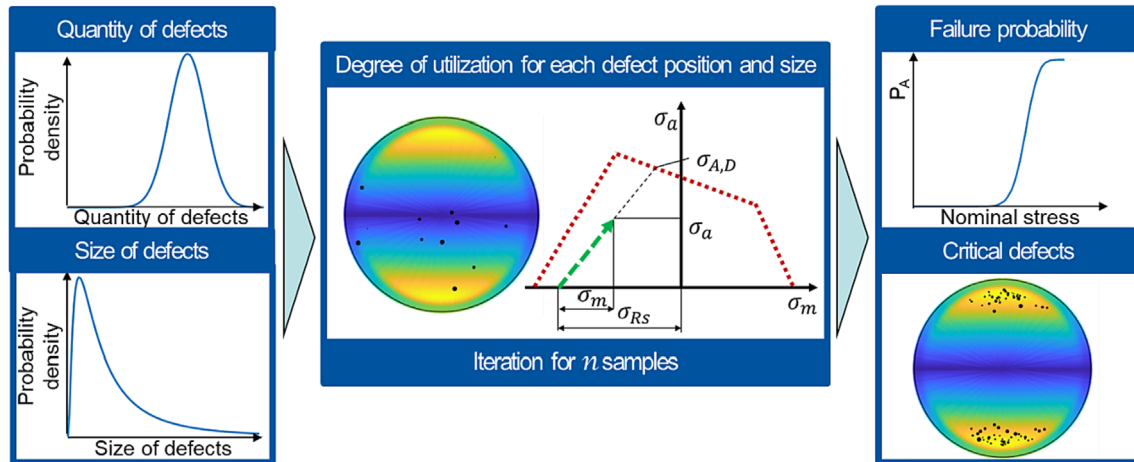
FIGURE 3 Input variables and schematic Monte Carlo calculation procedure for the fatigue strength of carburized samples according to Meis et al.[21] with consideration of material defects, using the example of the circular cross section of an unnotched round sample under axial bending loading. Defect sizes and positions are assigned to each virtual sample using probability functions in order to determine the sample's fatigue strength and subsequently generate statistical data for a large number of samples. [Colour figure can be viewed at wileyonlinelibrary.com]
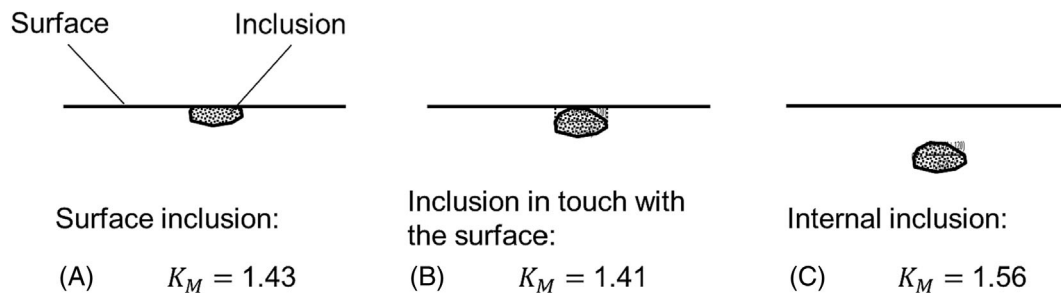
FIGURE 4 Reduction of fatigue strength due to the presence of non-metallic inclusions depending on the projected area of the defects and the local hardness for different defect positions, expressed by the factor K_M: (A) surface inclusion, (B) inclusion in touch with the surface, and (C) internal inclusion.[16]

considered. Murakami quantified the reduction of fatigue strength due to non-metallic inclusions, where the amount of strength reduction depends on the local hardness, the projected area of the defect, and on its position relative to the surface.[16] These findings are summed up in equation and Figure 4 and equation (3).

$$\sigma_w = K_M \cdot \frac{HV + 120}{(\sqrt{area})^{\frac{1}{6}}} \qquad (3)$$

Model inputs are statistical distributions of the positions and sizes of non-metallic inclusions in the steel component. The user should provide the volume concentration of inclusions and the general size distribution function in the raw material, whereas the positions are considered to be uniformly distributed. The determination of the distribution of sizes is a difficult task. Due to measurement methods that produce disparities between the seen and real values in frequency as well as in sizes of the material defects, the use of 2D micrographs with a constrained surface of analysis does not enable a reliable assessment of the original 3D statistics of relatively rare impurities in the steel. Extreme value statistics that take into account the observed volume and mathematical correction for slicing effects from 2D micrographs can help to partially solve these issues,[16,28,45] but choosing the right parameters for these situations necessitates a thorough analysis and can vary significantly depending on the material under consideration. The method put forth in Meis et al.[21] treats the distribution function for defect sizes and the concentration in defects as an input that can be easily changed, allowing one to calculate the fatigue strength of carburized components based on these parameters with a very small computational effort. This makes it possible to determine the assumptions for distribution of material flaws that produce realistic findings and to quantify the sensitivity of the fatigue strength forecast to the presence of defects.

Among the major advantages of the presented approach, the calculation results for fatigue strength of carburized components not only include the fatigue strength limit depending on several parameters such as the heat-treatment process and the material quality but also provides some insights on the failure statistics at different load levels and on the most likely position for crack initiation. It should be noted that while the approach described in Meis et al.[21] allows for the consideration of surface oxidation or residual stresses due to shot-peening, these effects are not included in the current work.
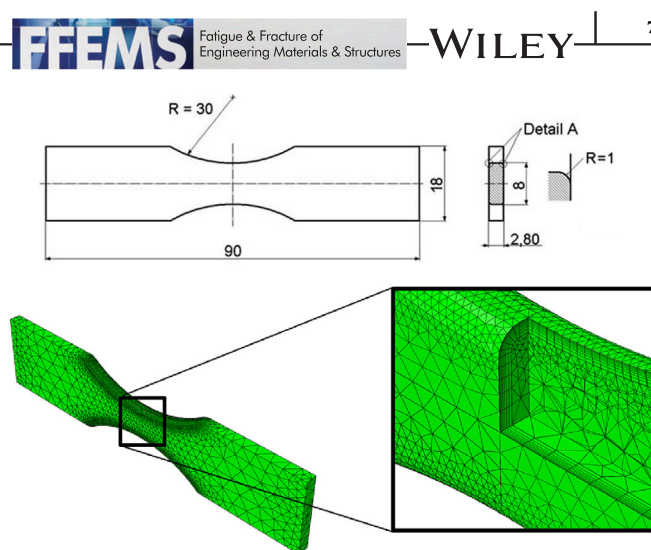

FIGURE 5 Geometry of the bending samples in Stöberl et al.[46] and features of the corresponding FE mesh. Displayed lengths are in mm. [Colour figure can be viewed at wileyonlinelibrary.com]

3 | VALIDATION OF THE DEVELOPED METHOD WITH EXPERIMENTAL RESULTS FROM LITERATURE

Experimental results published by Stöberl et al.[46] can be used to validate the developed approach. In this work, the endurance limit of carburized and carbonitrided specimens under axial bending was determined for fatigue ratio R = −1 and R = 0. The FE heat-treatment model provided in Iss et al.[25] can be used, and its predictions of phase composition, hardness, and residual stress distribution in the samples can be verified, thanks to the very comprehensive description of the heat-treatment conditions and residual stresses in Stöberl et al.[46] Figure 5 shows the samples' geometrical characteristics.

The simulation model published in Iss et al.[25] was used to simulate the heat treatment of the bending samples using the process settings described in Stöberl et al.[46] for the carburized samples of 18CrNiMo7-6 steel. The 82,000 linear wedge elements and 30,000 linear tetrahedral elements that make up the three-dimensional FE mesh have been refined towards the sample's outer surfaces in order to accurately capture the gradients in cyclic load stresses as well as carbon concentration, temperature, hardness, and residual stresses brought on by the heat treatment. The simulation is conducted in the FE program Abaqus[37] with user-defined FORTRAN subroutines to describe the evolution of phase transformations and strains in the material. Some characteristics of the FE mesh utilized for the bending sample geometry are shown in Figure 5, where a view cut has been applied on 1/4 of the detail picture in order to illustrate the inner structure of the mesh. Figure 6 displays the distribution
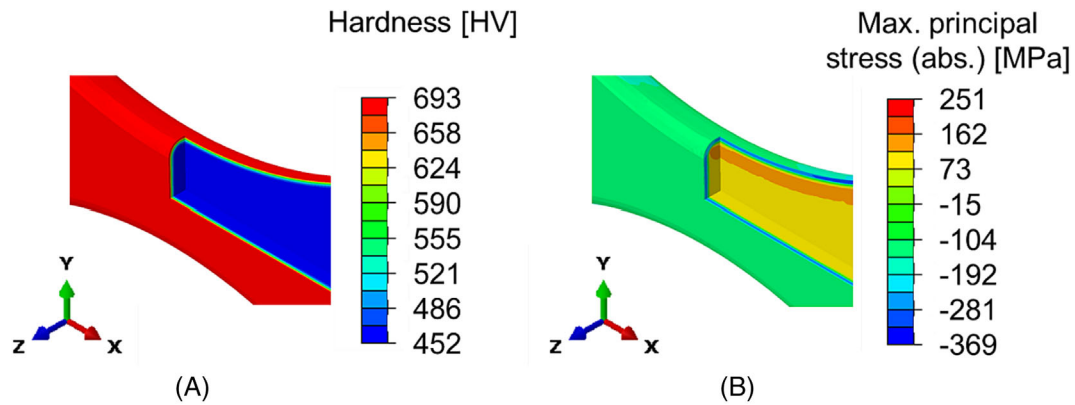
FIGURE 6 Simulation results of hardness (A) and residual stress gradients (B) in the carburized samples from Stöberl et al.[46] [Colour figure can be viewed at wileyonlinelibrary.com]
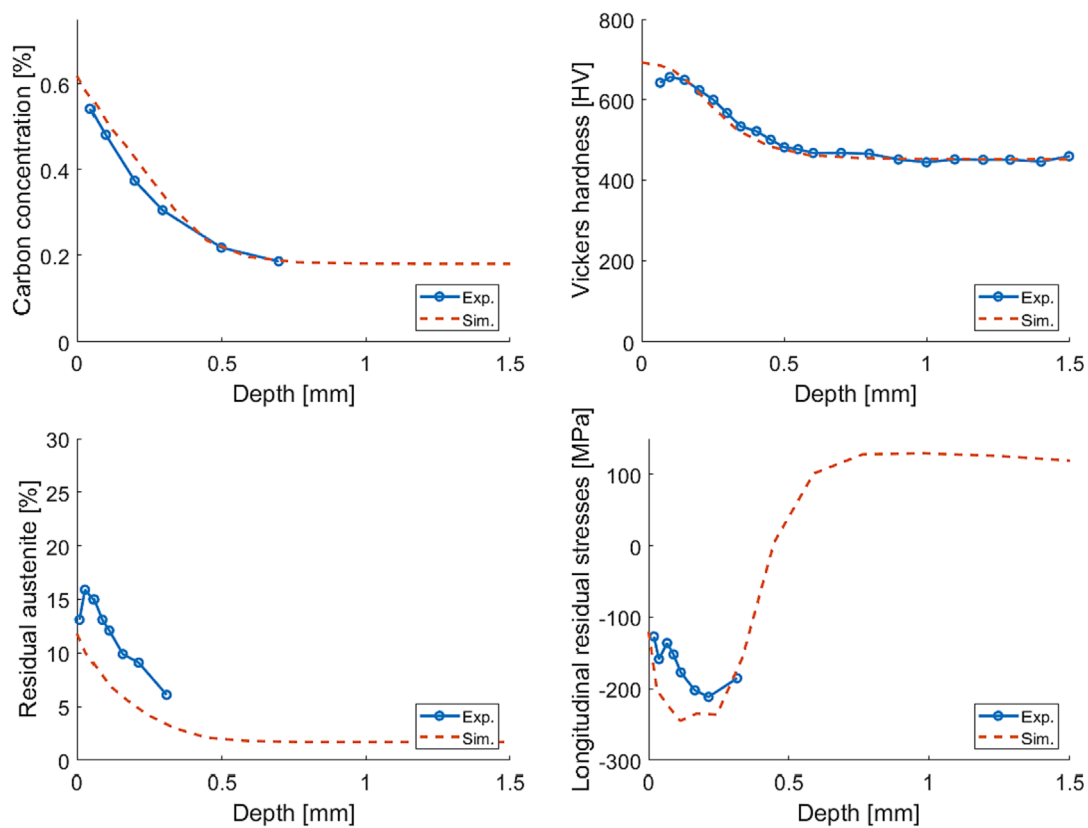
FIGURE 7 Comparison between experimental results from Stöberl et al.[46] and simulation results from present work for carbon concentration, hardness, residual austenite volume fraction, and residual stress profiles. [Colour figure can be viewed at wileyonlinelibrary. com]

of hardness and residual stresses in the sample, where the residual stress tensor is represented by its principal stress with the maximum absolute value. The typical residual stress gradients for carburized components can be observed, with compressive residual stresses in the case and tensile stresses in the core material. On a path normal to the carburized surface, Figure 7 compares experimental and simulation data for the sample's carbon

content, hardness, volume fraction of residual austenite, and residual stresses.

The FE-based model can be considered as a prediction tool with sufficient accuracy to carry out the fatigue strength assessment of carburized samples because only minor differences in depth profiles of carbon concentration, hardness, residual austenite volume concentration, and longitudinal residual stresses can be observed

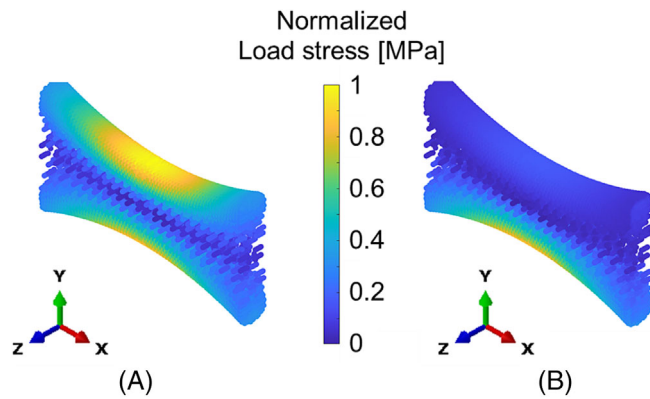**FIGURE 8** Calculated equivalent normalized load stress $\sigma_{eq,load,norm}\left(\vec{x}\right)$ of the discrete material points in the investigated notch region of samples from mechanical FE simulation of axial bending with stress ratio (A) R = −1 and (B) R = 0. Details for the calculation of this variable are available in Appendix A. [Colour figure can be viewed at wileyonlinelibrary.com]

FIGURE 9 Size distribution function assumptions for non-metallic inclusions, applied for a total material volume of 4000 mm³ and the respective volume concentration values described above. [Colour figure can be viewed at wileyonlinelibrary.com]

between the data from simulation and experiment. These minor variations seem to have some connection to the low predicted austenite phase fraction. This could be adjusted by calibrating the parameters used in the Koistinen–Marburger model[41] or for calculation of the martensite start temperature M_s.

The identical geometry and mesh used in the heat-treatment process are then used to simulate the mechanical loading of the bending samples in the FE program Abaqus.[37] One of the ends of the sample is fixed by prescribing constant values for all mechanical degrees of freedom, and the load is defined by a unit bending moment. For stress ratios R = −1 and R = 0, the load amplitude is defined throughout the course of a whole cycle. Only elastic material behavior is taken into account in this step. The normalized equivalent load stresses in the bending samples for the stress ratios R = −1 and R = 0 are computed in Matlab R2021[47] for every integration point and are shown in Figure 8. As expected, when specifying a stress ratio of 0, the sample is primarily loaded on one side, but alternating stresses with R = −1 are evenly distributed across both sides of the carburized sample.

Note that, in order to derive a scalar equivalent stress from the 3D time-varying stress tensor components, the normal stress hypothesis has been used here. The details of the calculation can be found together with the general flow chart of the probabilistic method for prediction of the fatigue strength of carburized samples in Appendix A. The calculation scheme selected in Appendix A implicitly presumes a proportional stress condition, which implies that the directions of the residual and load stresses match. Instead of performing the
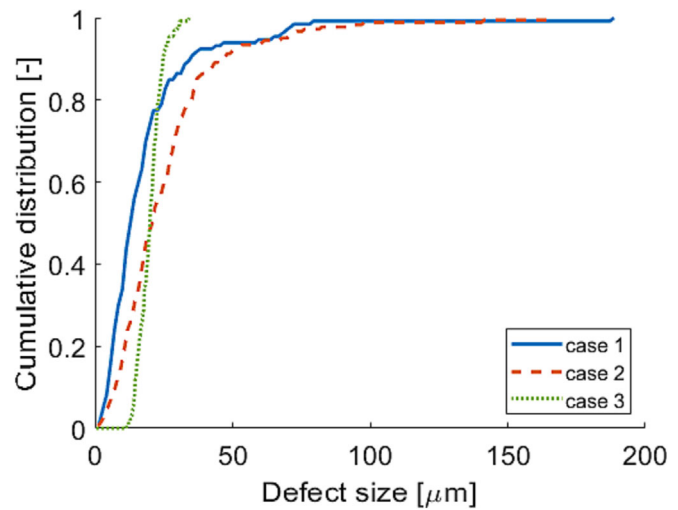
calculation of the local degree of utilization only once for all load levels, a more general approach consists of first directly adding together the stress tensors from residual stresses and load stresses. This would then require calculating the equivalent stress and degree of utilization separately for each load amplitude in order to determine the corresponding failure probability. Even though this strategy is viable, it can result in much longer calculation times. The mean stress sensitivity m at each position is defined according to FKM[14] depending on the local ultimate tensile stress R_m in MPa (Equation 4), which can be estimated from the local hardness HV using Equation (5).[48]

$$m = 3.5 \cdot 10^{-4} \cdot R_m - 0.1 \tag{4}$$

$$R_m = -8.4674 + 3.3398 \cdot HV - 7 \cdot 10^{-4} \cdot HV^2 + 1 \cdot 10^{-6} \cdot HV^3 \tag{5}$$

For the second calculation step, assumptions for the size distribution of defects in the material should be made. Based on the work of Wickborn[28] and on some own preliminary results, the following configurations will be investigated:

- Case 1: Generalized extreme value distribution with mean size $\mu_{dist} = 10$ μm, shape parameter $k_{dist} = 0.3$, scale parameter $\sigma_{dist} = 0.75 \cdot \mu_{dist}$, and volume concentration for defects $C_d = 0.035$ mm^{-3}

- Case 2: Generalized extreme value distribution with mean size $\mu_{dist} = 15$ μm, shape parameter $k_{dist} = 0.3$, scale parameter $\sigma_{dist} = 0.85 \cdot \mu_{dist}$, and volume concentration for defects $C_d = 0.050$ mm^{-3}
- Case 3: Lognormal distribution with mean size $\mu_{dist} = 20$ μm, shape parameter $k_{dist} = 0.3$, standard deviation $\overline{\sigma}_{dist} = 0.5 \cdot \mu_{dist}$, and volume concentration for defects $C_d = 0.035$ mm^{-3}.

The probability density function of the generalized extreme value distributions for size variables $x > 0$ can be found in Equation (6),[49] using the parameters defined above. The lognormal probability density function is expressed in Equation (7).

$$P(X \leq x) = \frac{1}{\sigma_{dist}} \cdot exp\left\{ -\left(1 + k_{dist} \frac{x - \mu_{dist}}{\sigma_{dist}} \right)^{\frac{-1}{k_{dist}}} \right\}$$
$$\cdot \left(1 + k_{dist} \cdot \frac{x - \mu_{dist}}{\sigma_{dist}} \right)^{\frac{-k_{dist}-1}{k_{dist}}} \text{ if } k_{dist} \neq 0 \quad (6)$$

$$P(X \leq x) = \frac{1}{\sigma_{dist}} \cdot exp\left\{ -exp\left(-\frac{x - \mu_{dist}}{\sigma_{dist}} \right) - \frac{x - \mu_{dist}}{\sigma_{dist}} \right\} \text{ if } k_{dist} = 0$$

$$P(X \leq x) = \frac{1}{x \cdot \sigma_{dist} \cdot \sqrt{2\pi}} \cdot exp\left(\frac{-\log(x - \mu_{dist})^2}{2 \cdot \sigma_{dist}^2} \right)^{k_{dist}} \quad (7)$$

Figure 9 displays the distribution functions adopted in cases 1–3, respectively. It should be noted that these decisions are partially arbitrary and only used to investigate the potential of the simulation model to predict the fatigue strength behavior depending on the presence of non-metallic inclusions. The parameters for the size distribution of defects should be fine-tuned in future studies to obtain quantitatively reliable calculation results.

The presence of non-metallic inclusions locally reduces the admissible stresses. The fatigue strength loss is dependent on both the size of the inclusion and the local material hardness, as shown by the equations of Murakami et al. in Figure 4. The position and admissible load of the most critical material point are determined using the updated values of local strength with consideration of non-metallic inclusions. This information is saved, and new random positions and defect sizes are then assumed based on the size distribution functions previously defined. This process is repeated until statistically significant results and convergence emerge. In this work, a number of 3000 iterations is shown to be sufficient and corresponds to a computing time of around 1 min for 500,000 material points. Appendix A summarizes in a flow chart the calculation procedure for the

fatigue strength of carburized parts developed in this work.

Figure 10, where the depicted defect size is magnified by a factor of 200 relative to the sample for clarity, shows the superposition of the computed critical non-metallic inclusions in 3000 bending samples for the stress ratios R = −1 and R = 0 and the size distribution for defects from "case 1". The majority of crack initiations are found to be in the most heavily loaded near-surface area, as expected. For R = 0, it appears that the vast majority of critical positions are on the loaded side, whereas samples that have undergone alternating bending strains exhibit a symmetrical failure pattern. It can be noted that sample failure also occasionally occurs in low-stress areas when there are exceptionally large defects present or substantial tensile residual stresses.

Although the quantitative comparison of the frequency of such failures between model and experiment has not yet been thoroughly analyzed, this feature correlates with experimental findings on steels with high hardness properties and adequate compressive residual stresses on the loaded surface. This feature also illustrates a promising potential of the developed probabilistic approach to predict rare failure events.

Figure 11 demonstrates that there is a threshold in the maximum permissible stress amplitude in the sample at which every sample is projected to fail, despite the fact that certain samples sometimes fail at much lower load levels due to large-sized defects. This threshold is equivalent to the simulation model's predicted maximum admissible stress under defect-free conditions. Figure 11 also presents the outcomes of a simulated staircase fatigue test using 25 randomly chosen virtual samples, which can be compared with the experimental findings from Stöberl et al.[46] With differences of 5–10%, the calculated and experimental values for fatigue strength are pretty closely correlated. It is stated in Stöberl et al.[46] that the majority of the sample failures for the carburized samples showed crack initiation near the surface and not at non-metallic inclusions. In fact, crack initiation at non-metallic inclusions is here not anticipated to be as critical as crack initiation brought on by surface roughness, surface oxidation, or failure of the martensite matrix due to the relatively limited loaded volume in the samples and standard cleanness of the steel. This explains the strong threshold behavior seen in the samples' simulated fatigue strength distribution, even though this impact would likely manifest under actual test settings in a considerably milder manner. Whether relevant findings can be achieved with the selected test data can be questioned here, since the developed method is mostly suitable for crack and failure initiation due to internal defects such as non-metallic inclusions. The authors are

FIGURE 10 Superposed size and position of the most critical non-metallic inclusion in 3000 virtual axial bending samples subjected to (A) alternating cyclic stresses (R = −1) and (B) cyclic stresses with mean stress (R = 0). For clarity, the displayed defect size is multiplied by 200 in relation to the sample. [Colour figure can be viewed at wileyonlinelibrary.com]

FIGURE 11 Prediction of the cumulative distribution of failure bending stress for 3000 virtual samples under (A) alternating cyclic stresses (R = −1) and (B) cyclic load with mean stress (R = 0) and comparison with the experimental values from Stöberl et al.[46] [Colour figure can be viewed at wileyonlinelibrary.com]

aware of this issue and acknowledge that exact quantitative validation based on available test data has not yet been fully achieved. Further arguments about the applicability of the method developed in this work as well as the model's validity restrictions are discussed in Section 4. The quality of the documentation of the heat treatment and fatigue testing in Stöberl et al.,[46] on the other hand, enables a precise replication of the whole simulation chain, including intermediate validation of, for example, residual stresses and hardness from carburizing heat treatment, which is not available from practically all other sources for steel 18CrNiMo7-6. Since a faithful description of the local hardness and residual stresses is required to predict the fatigue strength of carburized samples, the selected experimental data appear to allow drawing at least qualitative conclusions on the method's capability.

Figure 12 illustrates how the material quality affects the computed fatigue strength of the axial bending samples while taking into account the three different variations of inclusion volume density and size distribution previously discussed. Since the authors of the

experimental study insist that most sample failures do not feature a crack initiation at internal defects or non-metallic inclusions, it is challenging to evaluate the applicability of the assumptions for defect distributions for the observed heat-treatment and load conditions. However, Figure 12 suggests a plausible qualitative influence of the steel cleanliness on the fatigue strength of the carburized samples. The fatigue strength of the carburized samples is decreased by a rise in the number and size of non-metallic inclusions, both in fully reversed load cycles with R = −1 and in load cycles with mean stresses with R = 0. The higher loaded volume of the sample and resulting increased likelihood that a large-sized defect is present in the heavily loaded area (i.e., the statistical size effect) explain why the influence of the material quality appears to be greater for samples loaded with R = −1 than for samples loaded with R = 0. Although this may vary when taking into account a larger sample volume, the lognormal size distribution of case 3 seems to result in a similar fatigue strength as the distribution function for case 1. In fact, it is anticipated that the generalized extreme values of case 1's distribution function will

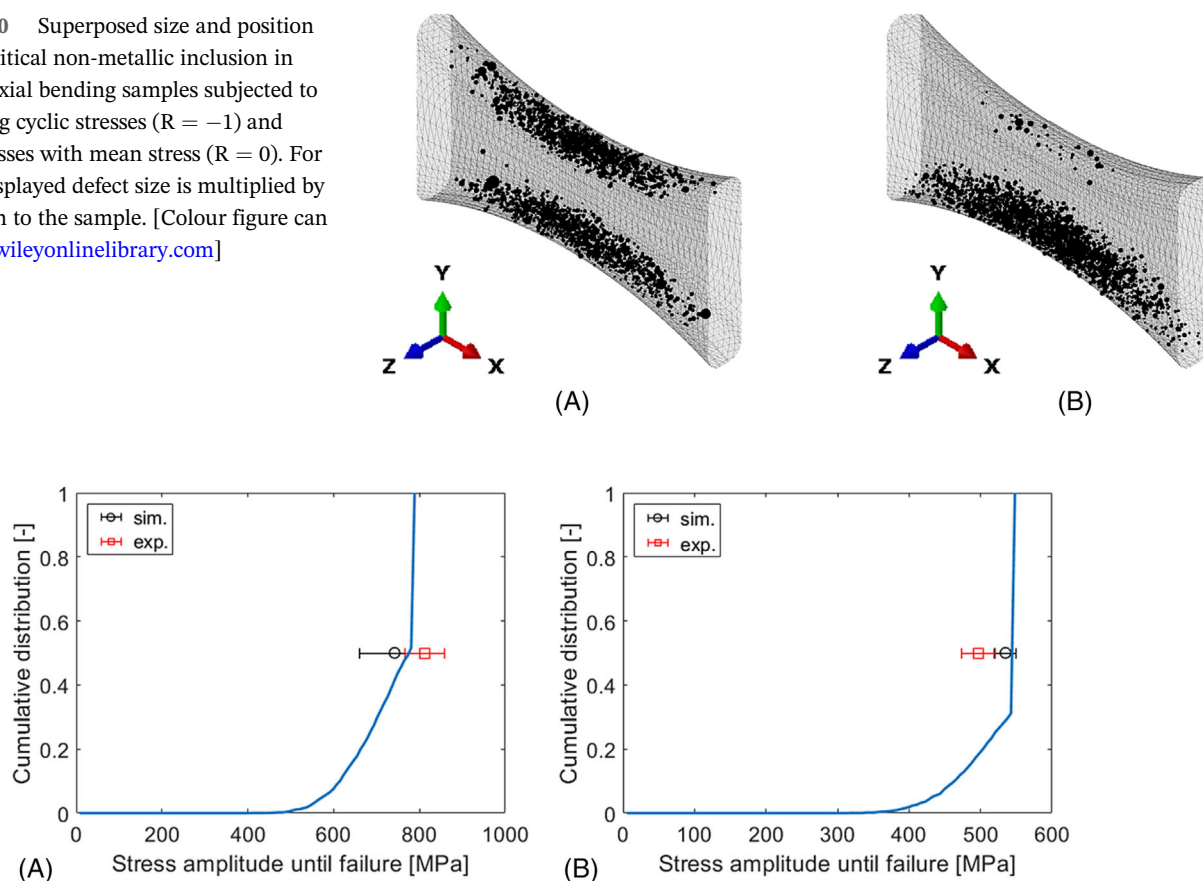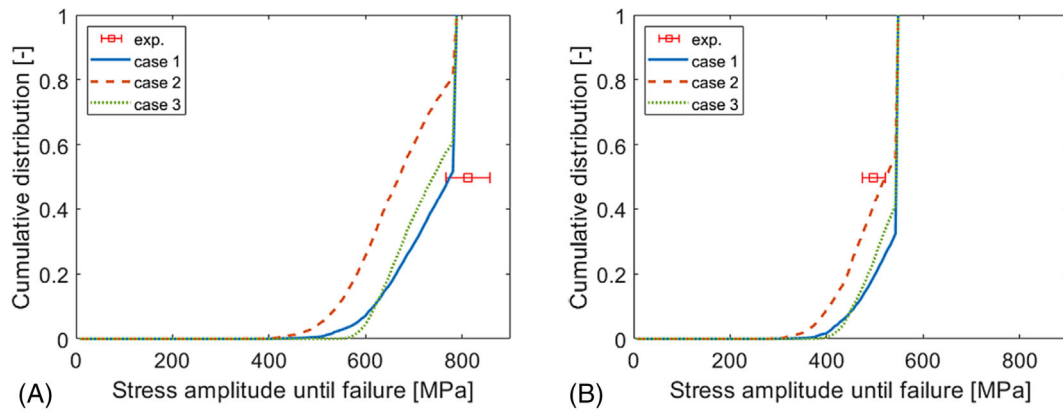**FIGURE 12** Prediction of the cumulative distribution of failure bending stress for 3000 virtual samples under alternating cyclic stresses (R = −1, left) and cyclic stresses with mean stress (R = 0, right) resulting from different assumptions on the distribution of material defects. [Colour figure can be viewed at wileyonlinelibrary.com]

occasionally show extremely large inclusion sizes, which are particularly harmful to fatigue strength. In comparison to the lognormal function of scenario 3, the chance of such events increases with the sample volume and loaded volume at a faster rate for the generalized extreme value function.

Although it is difficult to assess quantitatively the accuracy of every aspect of the developed simulation-based approach, the case-study based on experimental results from literature shows meaningful results regarding the predicted fatigue strength values, consideration of load, and heat-treatment conditions as well as on the effects of non-metallic inclusions for carburized samples. In the next section, the presented model is used in a study to numerically predict the fatigue strength of carburized round samples subjected to rotating bending load as a function of both geometry, case hardening depth, and material quality.

4 | SIMULATIVE STUDY ON THE PREDICTION OF ROTATING BENDING STRENGTH OF CARBURIZED SAMPLES

In this section, a simulative study is carried out in order to evaluate the fatigue strength behavior of carburized components as a function of geometry, heat-treatment parameters, and steel cleanliness. This study demonstrates the potential of the presented approach in understanding complex interactions between the influencing factors and derive some useful insights for coordinated optimization of manufacturing route, material choice, and mechanical design.

Object of the study are the three geometries of round fatigue samples presented in Appendix B. The sample's base geometry presents a diameter of 10 mm and a length of 32 mm for the examined area. Two notched samples with notch depths of 1 mm and notch radii of 10 and 4 mm are used in the numerical investigation to simulate additional variations in the local load amplitude and load concentration. The CHD, which represents the distance from the surface at which a hardness of 550 HV is attained, is changed for each geometry between 0 and 1.5 mm in steps of 0.25 mm. For the carburizing process, the FE model from Iss et al.[25] mentioned in the previous section is utilized to compute the hardness and residual stresses of heat-treated samples of 18CrNiMo7-6 steel with various CHDs. The full three-dimensional geometries of the samples are created in Abaqus 2020 and meshed with a total number of 150,000 to 175,000 linear coupled thermal-mechanical elements C3D4T and C3D6T and refined in the near-surface region. The profiles of residual stress and hardness along the depth of the round, unnotched sample are shown in Figure 13 as a function of the CHD. For CHD = 0 mm, the hardness is assumed to be equal to 450 HV, and no residual stresses are considered. The simulation model indicates that as CHD increases, the residual stress profiles will move deeper into the material. Increased hardness depth reduces maximum compressive stresses in the near-surface region while increasing anticipated tensile residual stresses. These findings are consistent with the current understanding as described in other works.[1,24,25]

The mechanical simulation of the load stresses is also carried out in the software Abaqus 2020,[37] with the same geometry and mesh. The element types, however, have been changed to C3D4 and C3D6. The two following hypotheses and distribution functions from Section 3 were retained as illustrating two different material qualities of the case-hardening steel 18CrNiMo7-6 in order to model the impact of non-metallic inclusions on the
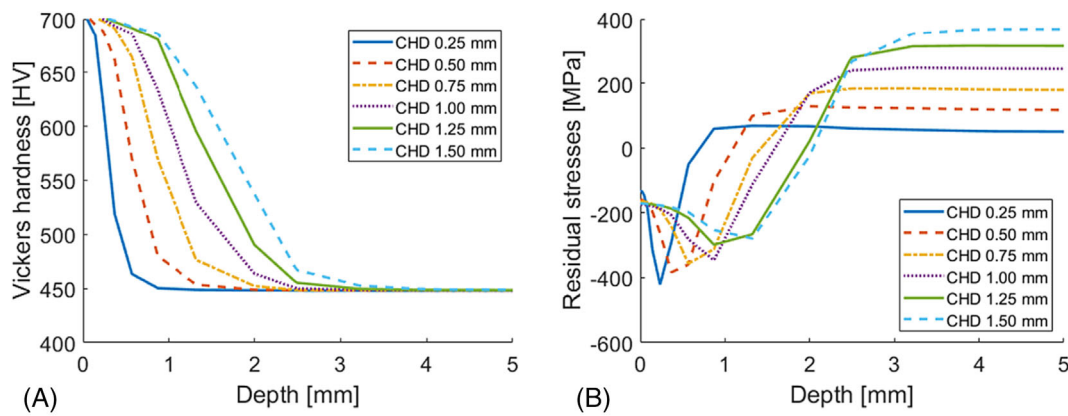
FIGURE 13 FE-based prediction of (A) hardness and (B) residual stress profiles, along the depth of unnotched carburized round samples with diameter 10 mm and varying case-hardness depth (CHD). [Colour figure can be viewed at wileyonlinelibrary.com]

FIGURE 14 Position of the most critical non-metallic inclusion in 3000 virtual unnotched samples with the case 1 assumption for non-metallic inclusion distribution and CHDs between 0 and 1.50 mm. [Colour figure can be viewed at wileyonlinelibrary.com]
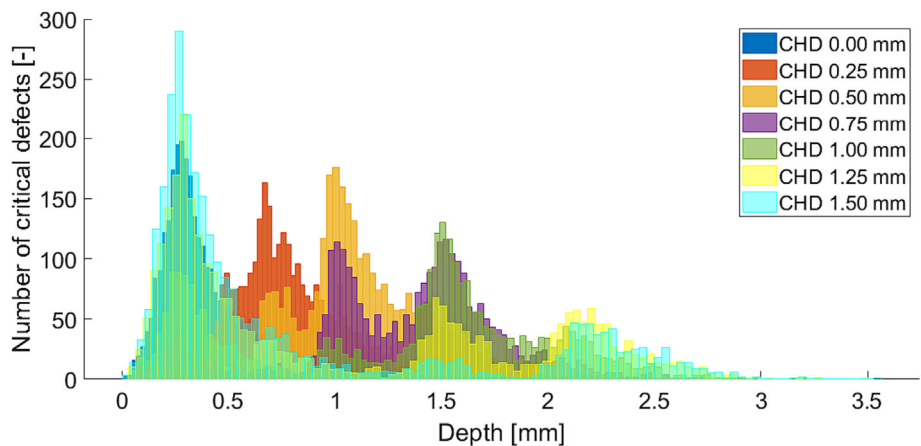
fatigue strength of the carburized samples under rotational bending load:

- Case 1: Generalized extreme value distribution with mean size $\mu_{dist} = 10$ μm, shape parameter $k_{dist} = 0.3$, scale parameter $\sigma_{dist} = 0.75 \cdot \mu_{dist}$, and volume concentration for defects $C_d = 0.035$ mm^{-3}
- Case 2: Generalized extreme value distribution with mean size $\mu_{dist} = 15$ μm, shape parameter $k_{dist} = 0.3$, scale parameter $\sigma_{dist} = 0.85 \cdot \mu_{dist}$, and volume concentration for defects $C_d = 0.050$ mm^{-3}

Figures 14 and 15 show the computed distributions for the positions of non-metallic inclusions responsible for failure of 3000 virtual unnotched samples as a function of the CHD. As expected, higher CHD causes the area beneath the component's surface with enhanced hardness and advantageous compressive residual stresses to spread out, thus shifting the most critical positions for crack initiation towards greater material depths. For CHDs 1.0–1.50 mm, increased relative frequency of crack initiation in the near-surface region is caused by

the somewhat reduced compressive residual stresses in this region, whereas the beneficial compressive residual stresses cover the entire cyclically loaded area of the sample.

As shown in Figure 16A, the carburizing heat treatment is anticipated to increase the fatigue strength of rotational bending samples without notches. Increased fatigue strength is a result of higher CHD, albeit the effect tends to level off at about 1.25 mm. The model does not forecast appreciable strength gains for case hardening depths more than 1.25 mm for round, unnotched samples with a diameter of 10-mm subject to rotating bending. The CHD directly affects the process time and energy costs of conventional gas carburizing heat-treatments,[2] therefore knowing the ideal CHD for a certain component geometry can be highly useful information in the context of industrial operations. The quantity and size of material defects are among the impacting factors, and increasing steel purity results in significantly higher fatigue strength of the carburized samples without notch.

Although carburized notched samples also experience the previously described effects, the degree of the
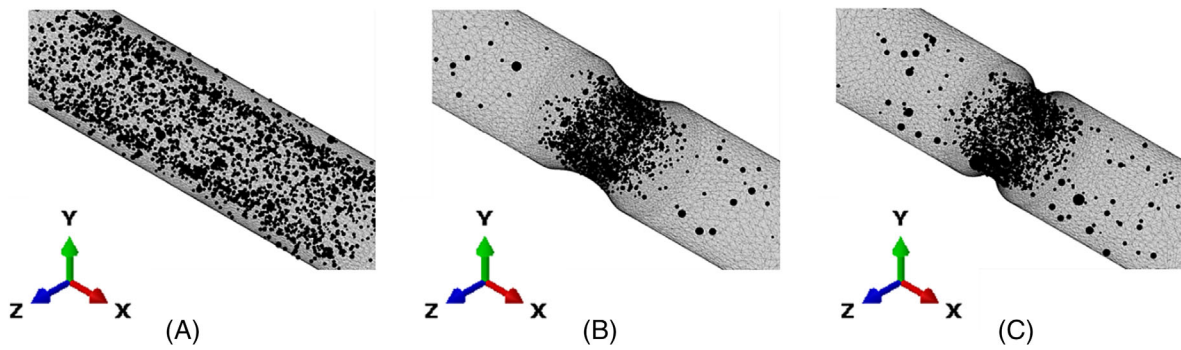
FIGURE 15 Position of the most critical non-metallic inclusion for 3000 superposed virtual round samples with the case 1 assumption for non-metallic inclusion distribution and CHD 0.75 mm. For clarity, the displayed defect size is multiplied by 200 in relation to the sample. (A) Unnotched sample, (B) sample with notch radius 10 mm, and (C) sample with notch radius 4 mm. [Colour figure can be viewed at wileyonlinelibrary.com]
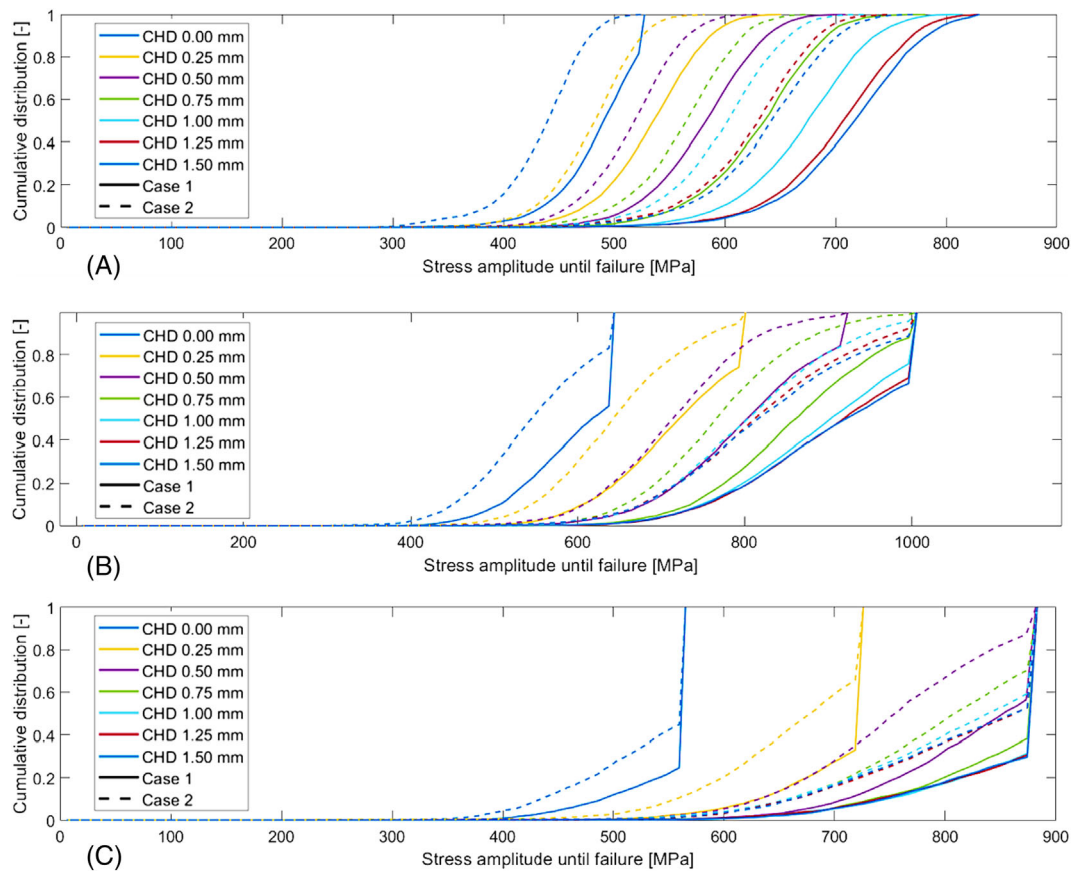
FIGURE 16 Cumulative distribution of fatigue strength for (A) unnotched samples, (B) samples with notch radius 10 mm, and (C) samples with notch radius 4 mm as a function of case-hardness depth (CHD) and material quality, where "case 1" and "case 2" represent the previously detailed assumptions for the distribution of non-metallic inclusions in the steel. [Colour figure can be viewed at wileyonlinelibrary.com]

increase in fatigue strength brought on by CHD and the material's quality seem to be strongly influenced by the sample's geometry. The samples with sharper notches, which are associated with smaller loaded volumes and higher stress concentrations, display a substantially higher sensitivity to minor increments in the CHD, as seen in Figure 16B,C. A more accurate evaluation of these variations is possible by plotting the estimated
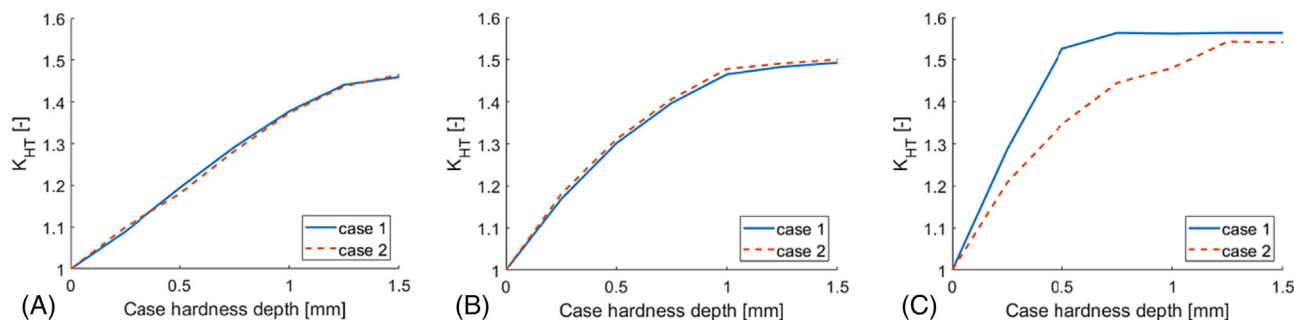
FIGURE 17 Plot of the strengthening factor K_{HT} for fatigue strength under rotating bending for (A) unnotched samples, (B) samples with notch radius 10 mm, and (C) samples with notch radius 4 mm as a function of case-hardness depth (CHD) and material quality. [Colour figure can be viewed at wileyonlinelibrary.com]

TABLE 1 Strengthening factor K_{HT} for carburized specimens depending on the geometry as specified in FKM guidelines,[14] range of validity 0.2 mm ≤ CHD ≤ 0.8 mm.

Specimen diameter	Unnotched specimen	Notched specimen
8–15 mm	1.2–2	1.5–2.5
30–40 mm	1.1–1.5	1.2–2

stresses for 50% failure probability of the various samples as a function of the CHD. Figure 17 shows the strengthening factor K_{HT} for the examined sample geometries. K_{HT} is calculated as the ratio between the load stress amplitude for 50% failure probability for the same samples after carburizing heat treatment and after blind-hardening, respectively, as described in Equation (8):

$$K_{HT} = \frac{\sigma_{a,D}}{\sigma_{a,D}(CHD = 0\,mm)} \tag{8}$$

All of the examined geometries seem to be affected similarly by the carburizing heat treatment, regardless of the material quality, with fatigue strength increases up to 55% in the investigated range. However, it is projected that small CHDs will more significantly enhance the fatigue strength of samples with sharp notches. While unnotched samples can benefit from CHDs beyond 1.25 mm, samples with notch radius 4 mm and the defect distribution from assumption case 1 are nearly at their maximum fatigue strength with CHD = 0.50 mm. Carburizing heat treatment appears to be more efficient to increase the fatigue strength of samples with sharp notches when the material quality is higher.

As shown in Table 1, the outcomes of the developed probabilistic and FE-based calculation model support well the recommendations in FKM[14] for the anticipated increase in fatigue strength due to carburizing heat treatment, although the predicted strengths tend to be in the lower value range. This study, however, provides a more detailed evaluation of the main influencing factors, allowing for a more accurate and targeted prediction of the fatigue strength of complex-shaped components. In contrast, the FKM guidelines[14] do not explicitly take into account the CHD, the material quality, or the coupling between these factors and only give a wide range of expected values for the surface strengthening.

The findings of this study merely show the method's potential for evaluating the fatigue strength of carburized components. They are not intended to serve as an explicit guideline for the design of mechanical parts or the heat-treatment procedure. In fact, some of the computation model's assumptions still need to be verified or improved. The challenge of assessing the volume concentration and the size distribution function of defects in the raw material is not fully addressed in this work. In addition, future models should take into account the effects of surface quality, grain size distribution, and intergranular oxidation, which have not yet been modeled. However, the flexibility, versatility, and low computational costs of the developed method open up a lot of opportunities as a tool for designing mechanical components and heat-treatment procedures. Large-scaled simulation studies could make it possible to analyze in-depth and very economically all significant influencing factors and their complex interactions. Therefore, it is possible to envision future standards like FKM,[14] DIN 743,[12] or ISO 6336[13] being based not only on theoretical foundations and sparse experimental research but also on an extensive database of results from validated simulation models. In recent years, FE-based models for calculating residual stresses and local hardness from heat-treatment processes like induction hardening,[29] carbonitriding,[50] or nitriding[51] have been developed. Combining these models with the probabilistic framework for fatigue strength

presented in this work may yield interesting insights into the interactions between residual stress distribution, surface hardening, and size effect associated with component geometry and material quality. However, unlike carburized components, induction hardened or nitrided parts rarely exhibit subsurface initiated fatigue failure due to non-metallic inclusions, thus requiring a more precise description of the surface state and limiting the benefits of probabilistic methods. Shot-peened components, on the other hand, exhibit higher strength near the surface due to strain hardening and high compressive residual stresses, shifting crack initiation to nonmetallic inclusions, and defects in the subsurface area.[2] Therefore, the authors consider that combining the current probabilistic fatigue strength approach with an additional empirical or FE-based calculation of the residual stresses induced by shot-peening processes could lead to improved models for safe fatigue design for industry-relevant carburized and shot-peened parts.

5 | SUMMARY AND CONCLUSION

Carburizing heat treatment represents a usual and very effective way of improving the fatigue strength of steel components. However, there are numerous influencing factors at play, including material quality, part geometry, hardness, and residual stress gradients created by the carburizing and quenching process conditions. In this work, a method based on a probabilistic evaluation of the positions and sizes of defects as well as a FE-based calculation of the heat treatment and mechanical fatigue loading of components is developed. Using experimental studies on axial bending fatigue on carburized samples of 18CrNiMo7-6 steel from Stöberl et al.,[46] the method is partially verified. Then, a simulated case study of the rotating bending fatigue of round carburized samples with and without notches and with varying material quality and CHD is used to illustrate the method's potential. These results can be summarized as follows:

- For axial bending fatigue of carburized samples under various load conditions, the proposed approach offers good qualitative agreement with the existing experimental work. In comparison to the experimental data, the gradients of carbon content, hardness, and residual stresses could be faithfully replicated, and the prediction of fatigue strength with stress ratios R = −1 and R = 0 fits within a 10% error margin.
- As shown in the case of rotating bending of notched and unnotched round samples, extensive simulative studies can be carried out in a very cost-effective

manner to explore the impact of key parameters on the fatigue strength of carburized components.

- Based on the CHD and notch radius, fatigue strength improvements for the assessed geometries relative to blind-hardened samples ranged from 10% to 55%.
- The CHD is projected to modify where the main crack-initiation spots are located. The crack initiation locations are shifted to increasing depths as a result of increased CHD. However, when the entire loaded region is covered by compressive residual stresses, reduced compressive residual stresses at the surface associated with high CHDs can raise the relative probability of crack formation in the near-surface region again.
- It appears that case hardening will work better for shallow CHDs when the samples have sharp notches than when they do not. Although a saturation behavior arises and is dependent on the sharpness of the notch, for the examined geometries and CHDs, an increase in CHD primarily resulted in a further improvement of the fatigue strength.
- It is predicted that large non-metallic inclusions will significantly reduce the fatigue strength of carburized samples, particularly when the loaded material volume is large or when infrequent failures at low stress levels are to be considered.

Several significant influencing variables, such as the surface roughness and the intergranular oxidation, have not yet been taken into account. This means that the conclusions made from the presented simulation models are not generalizable and that further research in these areas is required. Steel part fatigue properties encompass multiple possible failure causes, only the most likely of which occur during testing or service life. For carburized components with appropriate surface quality, considering solely fatigue failure caused by internal defects such as non-metallic inclusions may be a reasonable assumption. When working with parts with high surface roughness, deep oxidation, or low compressive residual stresses at the surface, however, the current method may result in a significant overestimation of the fatigue limit.

Still, the model developed in this work has been shown to generate a quantitatively satisfying prediction of the fatigue strength of the investigated complex-shaped carburized components. The effects of the material quality, the CHD, and the geometry on the fatigue properties of heat-treated samples could be computed and agree faithfully with the state of the art, thus enabling to estimate with accuracy the fatigue strength of carburized components with specific geometry features, steel cleanliness, or heat-treatment conditions. Further enhancements and verifications of the simulation model may

offer a very flexible and effective tool for joint optimization of mechanical design and heat-treatment process conditions.

AUTHOR CONTRIBUTIONS

Valérian Iss: methodology, investigation, writing—original draft. Jean-André Meis: methodology, writing—review & editing. Ali Rajaei: supervision. Bengt Hallstedt: writing—review & editing. Christoph Broeckmann: funding acquisition. All authors have read and agreed to the published version of the manuscript.

CONFLICT OF INTEREST STATEMENT

The authors declare that they have no known competing financial interests or personal relationships that could have appeared to influence the work reported in this paper.

ACKNOWLEDGEMENTS

DATA AVAILABILITY STATEMENT

The data that support the findings of this study are available from the corresponding author upon reasonable request.

NOMENCLATURE

CHD	case hardening depth
DIN	German Institute for Standardisation
Exp.	experiment
FE	finite-element analysis
FKM	Forschungskuratorium Maschinenbau
HV	Vickers hardness
HSV	highly stressed volume
ISO	International Organization for Standardization
Sim.	simulation
A	local material utilization
A_d	local material utilization at defect position
C_d	concentration of defects in raw material
k_{dist}	shape parameter for distribution function of size of non-metallic inclusions
K_M	Murakami factor for fatigue strength reduction depending on the position of a defect
m	mean stress sensitivity
M_S	martensite start temperature
N_d	total number of defects in carburized part
P_A	probability of failure
R	stress ratio
R_m	ultimate tensile stress
$t_{8/5}$	cooling time between 800°C and 500°C
$\vec{x}$	coordinate vector

$\sqrt{area}$	square root of the inclusion area projected normal to the maximum principal stress direction
ε^{total}	strain tensor
ε^{el}	elastic part of the strain tensor
ε^{pl}	plastic part of the strain tensor
ε^{th}	thermal part of the strain tensor
ε^{tr}	phase transformation induced part of the strain tensor
ε^{trip}	phase transformation induced part of the strain tensor
ε^{cr}	creep part of the strain tensor
μ_{dist}	mean size of non-metallic inclusions
σ_a	stress amplitude
$\sigma_{a,D}$	fatigue limit
$\sigma_{a,load,\varphi,\theta}$	equivalent load stress amplitude in the material plane (φ,θ)
σ_{dist}	scale parameter for generalized extreme value size distribution function of size of non-metallic inclusions
$\overline{\sigma}_{dist}$	standard deviation for lognormal size distribution function of size of non-metallic inclusions
$\sigma_{eq,load,\varphi,\theta}$	equivalent scalar load stress in the material plane (φ,θ)
$\sigma_{eq,load}$	equivalent scalar load stress
$\sigma_{eq,load,norm}$	normalized equivalent scalar load stress
σ_m	mean stress
$\sigma_{m,load,\varphi,\theta}$	equivalent mean load stress in the material plane (φ,θ)
σ_N	nominal stress amplitude of external load
$\sigma_{N,max}$	maximum permissible nominal stress amplitude of external load
$\overline{\overline{\sigma}}_{RS}$	residual stress tensor
σ_{RS}	equivalent residual stress
σ_w	fatigue strength under fully reversed load
$\sigma_{w,load,RS}$	fatigue strength under fully reversed load and residual stresses
$\sigma_{w,load,RS,d}$	fatigue strength under fully reversed load and residual stresses at defect position
σ_{wu}	upper limit for fatigue strength under fully reversed load and without material defects
φ,θ	rotation angles for characterization of a material plane.

ORCID

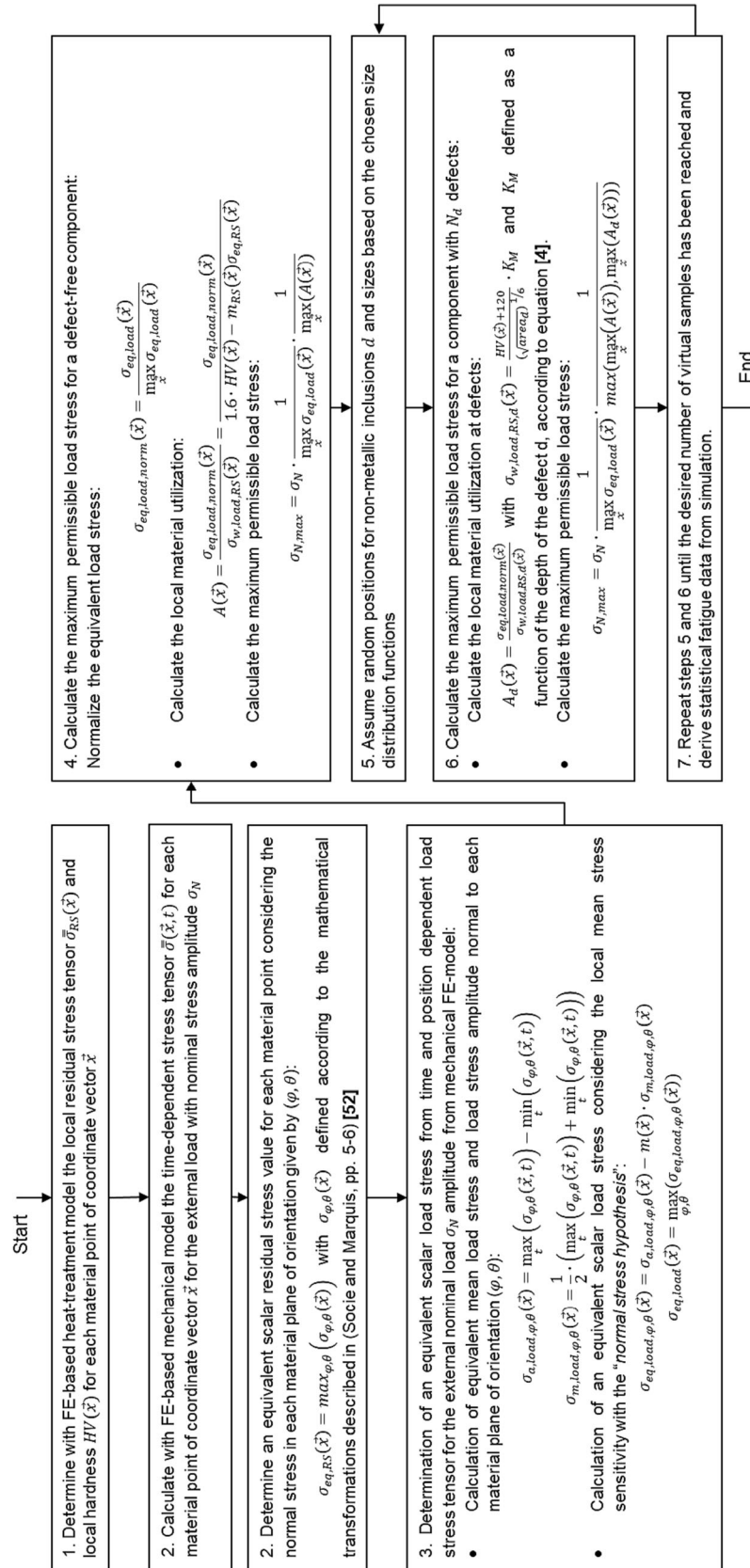*Bengt Hallstedt* https://orcid.org/0000-0001-5959-7030

REFERENCES

1. Réti T, Totten G, Howes M, Inoue T. Residual stresses in carburized, carbonitrided, and case-hardened components. In: *Handbook of Residual Stress and Deformation, ASM International*; 2002:189-210. doi:10.1361/hrsd2002p189

2. Davis JR. *Gear Materials, Properties, and Manufacture*. ASM international; 2005.

3. Milella PP. *Fatigue and Corrosion in Metals*. Springer Science & Business Media; 2012. doi:10.1007/978-88-470-2336-9

4. Spickenreuther M. *Untersuchungen zur Berechnung der Dauerfestigkeit von randschichtgehärteten Dieseleinspritzdüsen*. Doctoral dissertation,. Ilmenau Techn. Univ.; 2007. (in German).

5. Diemar A. *Simulation des Einsatzhärtens und Abschätzung der Dauerfestigkeit einsatzgehärteter Bauteile*. Doctoral dissertation,. Weimar university; 2007. (in German).

6. Lang OR. Dimensionierung komplizierter Bauteile aus Stahl im Bereich der Zeit- und Dauerfestigkeit. In: *Zeitung für Werkstofftechnik*. Vol.Nr. 10. Verlag Chemie GmbH, Weinheim; 1979 (in German). doi:10.1002/mawe.19790100108

7. Bruder T, Schön M. Durability analysis of carburized components using a local approach base on elastic stresses. *Materialwissenschaft und Werkstofftechnik: Mater Sci Eng Technol*. 2001; 32(4):377-387. https://onlinelibrary.wiley.com/doi/10.1002/1521-4052(200104)32:4<377::AID-MAWE377>3.0.CO;2-C

8. Grosch J. Fatigue resistance of carburized and nitrided steels. *Thermomech Surf Eng Steels*. 2015;209-240. doi:10.1533/9780857096524.2.209

9. Schleicher M, Bomas H, Mayr P. Berechnung der Dauerfestigkeit von gekerbten und mehrachsig beanspruchten Proben aus dem einsatzgehärteten Stahl 16MnCrS5. *HTM J Heat Treat Mater*. 2022;56(2):84-94 (in German). doi:10.1515/htm-2001-0024

10. Velten E. *Entwicklung eines Schwingfestigkeitskonzeptes zur Berechnung der Dauerfestigkeit thermochemisch randschichtverfestigter bauteilähnlicher Proben*. Doctoral dissertation. Technische Hochschule Darmstadt; 1984. (in German).

11. Kloos KH, Velten E. Einfluß einer Einsatzhärtung auf die Biegewechselfestigkeit bauteilähnlicher Proben. *HTM J Heat Treat Mater*. 1984;39(3):126-133 (in German). doi:10.1515/htm-1984-390306

12. DIN Deutsches Institut fur Normung e.V. *DIN 743. Tragfähigkeitsberechnung von Wellen und Achsen*. Beuth Verlag GmbH; 2012. (in German).

13. International Standardization Organization. *ISO 6336: Calculation of Load Capacity of Spur and Helical Gears*; 2006.

14. Rennert R. Frankfurt Forschungskuratorium Maschinenbau. Rechnerischer Festigkeitsnachweis für Maschinenbauteile aus Stahl. In: *Eisenguss-und Aluminiumwerkstoffen*. VDMA-Verlag; 2012. (in German).

15. Tridello A, Niutta CB, Berto F, Paolino DS. Size-effect in very high cycle fatigue: a review. *Int J Fatigue*. 2021;153:106462. doi:10.1016/j.ijfatigue.2021.106462

16. Murakami Y. *Metal Fatigue: Effects of Small Defects and Nonmetallic Inclusions*. Elsevier Science Ltd; 2002.

17. Zhu SP, Ai Y, Liao D, Correia JAFO, de Jesus AMP, Wang Q. Recent advances on size effect in metal fatigue under defects: a review. *Int J Fracture*. 2022;234(1-2):21-43. doi:10.1007/s10704-021-00526-x

18. Weibull W. *A Statistical Theory of Strength of Materials*. IVB-Handl; 1939.

19. Lai J, Lund T, Rydén K, Gabelli A, Strandell I. The fatigue limit of bearing steels—Part I: A pragmatic approach to predict very high cycle fatigue strength. *Int J Fatigue*. 2012;38:155-168. doi:10.1016/j.ijfatigue.2011.09.015

20. Konowalczyk P. *Grübchen- und Zahnflankenbruchtragfähigkeit großmoduliger Stirnräder: Pitting and Tooth Flank Fracture Load Capacity of Large Module Spur Gears*. Doctoral dissertation,. RWTH Aachen university; 2018. (in German).

21. Meis JA, Teklote F, Borowski M. Simulation of the tooth root strength under consideration of material quality, finishing process and size effects. In: *International Conference on Gears, VDI Berichte*. VDI Wissensforum GmbH; 2019. (in German).

22. Weber R. *Auslegungskonzept gegen Volumenversagen bei einsatzgehärteten Stirnrädern*. Doctoral dissertation,. Kassel university press; 2015. (in German).

23. Ruud C, Totten G, Howes M, Inoue T. Measurement of residual stresses. In: *Handbook of Residual Stress and Deformation*; 2002:99-117.

24. Witzig J. *Flankenbruch - eine Grenze der Zahnradtragfähigkeit in der Werkstofftiefe*. Doctoral dissertation,. Technische Universität München; 2012. (in German).

25. Iss V, Müller D, Haupt N. Erweiterte Berechnung der Flankenbruchtragfähigkeit unter besonderer Berücksichtigung des Eigenspannungszustands in größerer Werkstofftiefe. In: *FVA Forschungsvorhaben 835 I, Heft 1507, Forschungsvereinigung Antriebstechnik e.V*; 2021. (in German).

26. Böhme SA, Vinogradov A, Biermann H, Weidner A, Schmiedel A, Henkel S. Fatigue of carburised CrNiMo steel: testing and modelling concept. *Fatigue Fract Eng Mater Struct*. 2021;44(3):788-804, 2021-804. doi:10.1111/ffe.13394

27. Zuber D. *Fußtragfähigkeit einsatzgehärteter Zahnräder unter Berücksichtigung lokaler Materialeigenschaften*. Doctoral dissertation,. RWTH Aachen University; 2008. (in German).

28. Wickborn C. *Erweiterung der Flankentragfähigkeitsberechnung von Stirnrädern in der Werkstofftiefe*. Doctoral dissertation,. Technische Universtität München; 2017. (in German).

29. Tong D, Gu J, Totten GE. Numerical investigation of asynchronous dual-frequency induction hardening of spur gears. *Int J Mech Sci*. 2018;142:1-9. doi:10.1016/j.ijmecsci.2018.04.036

30. Castens M, Steinbacher M, Zoch HW. Vergleichbarkeit von Couponprobe und verzahntem Großgetriebebauteil. In: *FVA Forschungsvorhaben 501 III, Heft 1304. Forschungsvereinigung Antriebstechnik e.V.*; 2017. (in German).

31. Franz C, Lübben T, Lütjens J. Computational Aided Simulation of Heat Treatment (CASH) – Teil 3: Simulation der Einsatzhärtung komplexer Bauteilgeometrien durch Abstraktion. *ISIJ Int*. 2006;61(1):19-24. doi:10.3139/105.100360

32. Eser A, Broeckmann C, Simsir C. Multiscale modeling of tempering of AISI H13 hot-work tool steel–part 1: prediction of microstructure evolution and coupling with mechanical properties. *Comput Mater Sci*. 2016;113:280-291. doi:10.1016/j.commatsci.2015.11.020

33. Eser A, Broeckmann C, Simsir C. Multiscale modeling of tempering of AISI H13 hot-work tool steel–part 2: coupling predicted mechanical properties with FEM simulations. *Comput Mater Sci*. 2016;113:292-300. doi:10.1016/j.commatsci.2015.11.024

34. Diemar A, Hildebrand J, Gerth U, Könke C. Simulation-based optimization of the local material state in the field of cyclically highly stressed case hardened construction details with notch effect. *Mater Sci Eng Technol*. 2017;48(7):629-638. doi:10.1002/mawe.201600715

35. Scholzen P, Rajaei A, Brimmers J, Hallstedt B, Bergs T, Broeckmann C. Influence of heat treatment and densification on the load capacity of sintered gears. *Powder Metall*. 2023; 66(2):86-93. doi:10.1080/00325899.2022.2138171

36. Ehlers M, Gütler J, Schwarzer J. Computer aided simulation of heat treatment (CASH)—Teil 1: Ein Überblick. *HTM J Heat Treat Mater*. 2003;61(1):5-9. doi:10.3139/105.100358

37. Abaqus. 2020, *Dassault Systemes*. https://www.3ds.com/products-services/simulia/products/abaqus

38. Lütjens Z, Heuer V, König F, Lübben T, Schulze V, Trapp N. Computer aided simulation of heat treatment (CASH) Teil 2: Bestimmung von Eingabedaten zur FEM-Simulation des Einsatzhärtens. *HTM J Heat Treat Mater*. 2006;61(1):10-17. doi:10.3139/105.100359

39. Avrami M. Kinetics of phase change. Transformation-time relations for random distribution of nuclei. *J Chem Phys*. 1940;8(2): 212-224. doi:10.1063/1.1750631

40. Johnson W, Mehl R. Reaction kinetics in processes of nucleation and growth. *Trans Metall Soc AIME*. 1939;135:416-442.

41. Koistinen DP, Marburger RE. A general equation prescribing the extent of the austenite-martensite transformation in pure iron-carbon alloys and plain carbon steels. *Acta Metall*. 1959;7: 59-60.

42. Leblond JB, Devaux J, Devaux JC. Mathematical modelling of transformation plasticity in steels I: case of ideal-plastic phases. *Int J Plasticity*. 1989;5(6):551-572. doi:10.1016/0749-6419(89)90001-6

43. Leblond JB. Mathematical modelling of transformation plasticity in steels II: coupling with strain hardening phenomena. *Int J Plasticity*. 1989;5(6):573-591. doi:10.1016/0749-6419(89)90002-8

44. Garwood MF, Zurburg HH, Erickson MA. *Correlation of laboratory tests and service performance, interpretation of tests and correlation with service*. ASM; 1951.

45. Atkinson HV, Shi G. Characterization of inclusions in clean steels: a review including the statistics of extremes methods. *Progr Mater Sci*. 2003;48(5):457-520. doi:10.1016/S0079-6425(02)00014-2

46. Stöberl C, Bomas H, Clausen B, Hoffmann F, Zoch HW. Untersuchungen zur Dauerfestigkeit carbonitrierter Proben aus den Einsatzstählen 18CrNiMo7-6 und 20MnCr5: investigations on the endurance limit of carbonitrided specimens of case hardening steels 18CrNiMo7-6 and 20MnCr5. *Mater Sci Eng Dent Tech*. 2015;46(6):533-549 (in German). doi:10.1002/mawe.201500272

47. *MATLAB Version: 9.11.0 (R2021b)*. The MathWorks Inc. https://www.mathworks.com

48. International Standardization Organization, *DIN Deutsches Institut fur Normung e.V. 18265 DIN EN ISO 18265: 2014-02 Metallische Werkstoffe – Umwertung von Härtewerten*; 2014 (in German).

49. Kotz S, Nadarajah S. *Extreme Value Distributions: Theory and Applications*. World scientific; 2000. doi:10.1142/p191

50. Damon J. *Experimentelle und numerische Untersuchungen resultierender Randschichtzustände und Eigenschaften carbonitrierter pulvermetallurgisch hergestellter Bauteile*. Doctoral dissertation,. KIT Karlsruhe University; 2022. (in German).

51. Sawicki J, Siedlaczek P, Staszczyk A. Finite-element analysis of residual stresses generated under ntriding process: a three-dimensional model. *Metal Sc Heat Treatment*. 2018;59(11-12): 799-804. doi:10.1007/s11041-018-0229-y

52. Socie D, Marquis G. *Mutliaxial fatigue*. SAE International; 2000:5-6.

How to cite this article: Iss V, Meis J-A, Rajaei A, Hallstedt B, Broeckmann C. Fatigue strength evaluation of case-hardened components combining heat-treatment simulation and probabilistic approaches. *Fatigue Fract Eng Mater Struct*. 2023;1-21. doi:10.1111/ffe.14208

APPENDIX A: A FLOW CHART FOR PROBABILISTIC CALCULATION OF THE FATIGUE STRENGTH OF CARBURIZED SAMPLES

Start

1. Determine with FE-based heat-treatment model the local residual stress tensor $\bar{\bar{\sigma}}_{RS}(\vec{x})$ and local hardness $HV(\vec{x})$ for each material point of coordinate vector $\vec{x}$

2. Calculate with FE-based mechanical model the time-dependent stress tensor $\bar{\bar{\sigma}}(\vec{x},t)$ for each material point of coordinate vector $\vec{x}$ for the external load with nominal stress amplitude σ_N

2. Determine an equivalent scalar residual stress value for each material point considering the normal stress in each material plane of orientation given by (φ, θ):

$$\sigma_{eq,RS}(\vec{x}) = max_{\varphi,\theta}\left(\sigma_{\varphi,\theta}(\vec{x})\right) \text{ with } \sigma_{\varphi,\theta}(\vec{x}) \text{ defined according to the mathematical transformations described in (Socie and Marquis, pp. 5-6) [52]}$$

3. Determination of an equivalent scalar load stress from time and position dependent load stress tensor for the external nominal load σ_N amplitude from mechanical FE-model:

- Calculation of equivalent mean load stress and load stress amplitude normal to each material plane of orientation (φ, θ):

$$\sigma_{a,load,\varphi,\theta}(\vec{x}) = \max_t\left(\sigma_{\varphi,\theta}(\vec{x},t)\right) - \min_t\left(\sigma_{\varphi,\theta}(\vec{x},t)\right)$$

$$\sigma_{m,load,\varphi,\theta}(\vec{x}) = \frac{1}{2}\cdot\left(\max_t\left(\sigma_{\varphi,\theta}(\vec{x},t)\right) + \min_t\left(\sigma_{\varphi,\theta}(\vec{x},t)\right)\right)$$

- Calculation of an equivalent scalar load stress considering the local mean stress sensitivity with the "*normal stress hypothesis*":

$$\sigma_{eq,load,\varphi,\theta}(\vec{x}) = \sigma_{a,load,\varphi,\theta}(\vec{x}) - m(\vec{x})\cdot\sigma_{m,load,\varphi,\theta}(\vec{x})$$

$$\sigma_{eq,load}(\vec{x}) = \max_{\varphi,\theta}(\sigma_{eq,load,\varphi,\theta}(\vec{x}))$$

4. Calculate the maximum permissible load stress for a defect-free component: Normalize the equivalent load stress:

$$\sigma_{eq,load,norm}(\vec{x}) = \frac{\sigma_{eq,load}(\vec{x})}{\max_{\vec{x}}\sigma_{eq,load}(\vec{x})}$$

- Calculate the local material utilization:

$$A(\vec{x}) = \frac{\sigma_{eq,load,norm}(\vec{x})}{\sigma_{w,load,RS}(\vec{x})} = \frac{\sigma_{eq,load,norm}(\vec{x})}{1.6\cdot HV(\vec{x}) - m_{RS}(\vec{x})\sigma_{eq,RS}(\vec{x})}$$

- Calculate the maximum permissible load stress:

$$\sigma_{N,max} = \sigma_N\cdot\frac{1}{\max_{\vec{x}}\sigma_{eq,load}(\vec{x})}\cdot\frac{1}{\max_{\vec{x}}(A(\vec{x}))}$$

5. Assume random positions for non-metallic inclusions d and sizes based on the chosen size distribution functions

6. Calculate the maximum permissible load stress for a component with N_d defects:

- Calculate the local material utilization at defects:

$$A_d(\vec{x}) = \frac{\sigma_{eq,load,norm}(\vec{x})}{\sigma_{w,load,RS,d}(\vec{x})} \text{ with } \sigma_{w,load,RS,d}(\vec{x}) = \frac{HV(\vec{x})+120}{(\sqrt{area_d})^{1/6}}\cdot K_M \text{ and } K_M \text{ defined as a function of the depth of the defect } d, \text{ according to equation [4].}$$

- Calculate the maximum permissible load stress:

$$\sigma_{N,max} = \sigma_N\cdot\frac{1}{\max_{\vec{x}}\sigma_{eq,load}(\vec{x})}\cdot\frac{1}{max(\max_{\vec{x}}(A(\vec{x})),\max_{\vec{z}}(A_d(\vec{x})))}$$

7. Repeat steps 5 and 6 until the desired number of virtual samples has been reached and derive statistical fatigue data from simulation.

End

APPENDIX B: GEOMETRY OF ROUND SAMPLES FOR ROTATING BENDING FATIGUE